CHEMISTRY OF MATERIALS

Chemical Origin of in Situ Carbon Dioxide Outgassing from a Cation-Disordered Rock Salt Cathode

Tzu-Yang Huang, Zijian Cai, Matthew J. Crafton, Raynald Giovine, Ashlea Patterson, Han-Ming Hau, Justin Rastinejad, Bernardine L. D. Rinkel, Raphaële J. Clément, Gerbrand Ceder, and Bryan D. McCloskey*

Cite This: *Chem. Mater.* 2024, 36, 6535−6546

Read Online

ACCESS | Metrics & More | Article Recommendations | Supporting Information

ABSTRACT: In situ carbon dioxide (CO_2) outgassing is a common phenomenon in lithium-ion batteries (LiBs), primarily due to parasitic side reactions at the cathode−electrolyte interface. However, little is known about the chemical origins of the in situ CO_2 released from emerging Li-excess cation-disordered rock salt (DRX) cathodes. In this study, we selectively labeled various carbon sources with ^{13}C in cathodes containing a representative DRX material, $Li_{1.2}Mn_{0.4}Ti_{0.4}O_2$ (LMTO), and performed differential electrochemical mass spectrometry (DEMS) during galvanostatic cycling in a carbonate-based electrolyte. When charging LMTO cathodes, electrolyte solvent (EC) decomposition is the dominant source of the CO_2 outgassing. The amount of EC-originated CO_2 is strongly correlated with the total surface area of carbon black in the electrode, revealing the critical role of electron-conducting carbon additives in the electrolyte degradation mechanisms. In addition, unusual bimodal CO_2 evolution during the first cycle is found to originate from carbon black oxidation. Overall, the underlying chemical origin of in situ CO_2 release during battery cycling is highly voltage- and cycle-dependent. This work further provides insights into improving the stability of DRX cathodes in LiBs and is envisioned to help guide future relevant material design to mitigate parasitic reactions in DRX-based batteries.

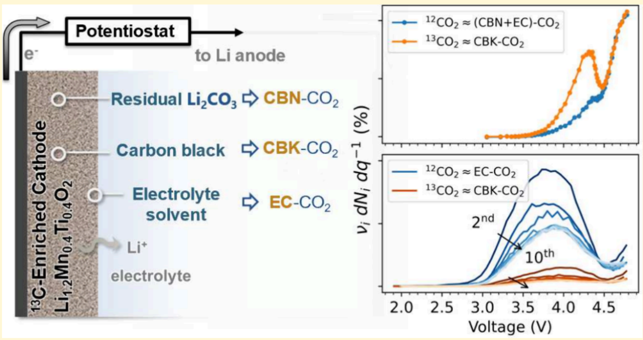

1. INTRODUCTION

The pursuit of efficient and sustainable energy storage systems has driven extensive research to improve lithium-ion batteries (LiBs). LiBs have emerged as the preferred choice for various applications due to their high energy density, long cycle life, and remarkable stability. These desirable properties are attributed to the intricate interplay of various components within LiBs, with the cathode playing a pivotal role. While conventional layered cathode materials, such as lithium nickel−manganese−cobalt oxides (NMC), have exhibited satisfactory performance, the limited availability of resources[1,2] and their high cost[3] have necessitated the exploration of alternative cathode materials with enhanced characteristics.

In recent years, cation-disordered rock-salt (DRX) materials[4−6] have garnered significant attention as potential cathode candidates for LiBs. These materials possess a disordered arrangement of cations within the rock-salt structure, providing greater design flexibility compared to that of their layered counterparts. The introduction of cation disorder not only enables the incorporation of earth-abundant transition metal (TM) chemistries but also allows the modulation of electrochemical properties.[7] However, as research on DRX cathodes progresses, a specific concern has emerged: severe carbon dioxide (CO_2) outgassing during battery operation.[8−10] In situ CO_2 outgassing refers to the release of carbon dioxide gas in a LiB during operation primarily due to parasitic side reactions at the cathode−electrolyte interface. Minimizing unwanted side reactions and stabilizing the electrode−electrolyte interface are crucial prerequisites for achieving long-term cycling of LiBs. Therefore, it is crucial to understand and address the impact of CO_2 outgassing on the performance and longevity of LiBs. In this context, the severity of the CO_2 outgassing of DRX cathodes becomes a critical concern.

However, our understanding of the outgassing of CO_2 in DRX cathodes remains limited. Previous investigations have predominantly focused on CO_2 outgassing from the surface of layered cathode materials,[11−13] while studies specifically addressing DRX materials are scarce. Therefore, the primary objective of this work is to address this knowledge gap by

Received: March 14, 2024
Revised: June 13, 2024
Accepted: June 14, 2024
Published: June 24, 2024

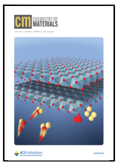

ACS Publications

https://doi.org/10.1021/acs.chemmater.4c00756

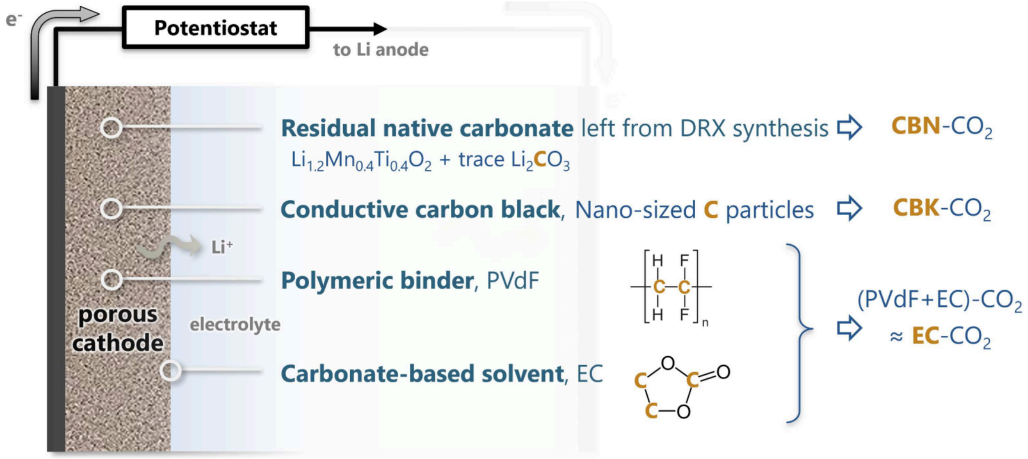

Figure 1. Schematics of probable carbon sources for CO_2 evolution from a porous DRX cathode. The nomenclature for CO_2 originated from each carbon source is indicated. The lithium anode side is made opaque to highlight CO_2 evolution from the DRX cathode side.

Table 1. List of LMTO Electrodes with Various ^{13}C-Labeled Carbon Sources

	isotopically labeled carbon sources			
LMTO electrode[a]	native carbonate	carbon black	electrolyte[b]	CO_2 source of interest
13CBN-12CBK	trace $Li_2{}^{13}CO_3$ (^{13}C-CBN)	Super C65, P (^{12}C-CBK)	ethylene carbonate (^{12}C-EC)	CBN-CO_2
13CBN-13CBK	trace $Li_2{}^{13}CO_3$ (^{13}C-CBN)	Sigma-Aldrich[c] (^{13}C-CBK)	ethylene carbonate (^{12}C-EC)	EC-CO_2
12CBN-13CBK	trace $Li_2{}^{12}CO_3$ (^{12}C-CBN)	Sigma-Aldrich[c] (^{13}C-CBK)	ethylene carbonate (^{12}C-EC)	CBK-CO_2

[a]Numeric 12 or 13 encodes the isotopic abundance in CBN or CBK. [b]1 M $LiPF_6$ in natural C abundance ethylene carbonate (EC). [c]^{13}C -enriched carbon powder sourced from the vendor, Sigma-Aldrich.

studying the in situ CO_2 outgassing from a representative DRX material, $Li_{1.2}Mn_{0.4}Ti_{0.4}O_2$ (LMTO). Our investigation aims to elucidate the underlying chemical origins of CO_2 generation, quantify the amount of CO_2 released from various sources during battery cycling, and evaluate its impact on the electrochemical performance and stability of the cathode—electrolyte interface.

To achieve these objectives, we implemented ^{13}C isotope labeling of various cell components to isolate and identify each probable carbon source for CO_2 evolution at the cathode—electrolyte interface. Additionally, we employ in situ gas analysis via differential electrochemical mass spectrometry (DEMS) to accurately decouple the contributions of the various carbon sources to the overall CO_2 release during battery cycling. Our analytical workflows provide real-time monitoring of CO_2 evolution, enable correlation of CO_2 outgassing with the electrochemical behavior of the cathode, and facilitate identification of the chemical origins of CO_2. By shedding light on the distinct challenges posed by the outgassing of CO_2 from DRX cathodes, this study contributes to the development of strategies to mitigate and control this phenomenon.

2. RESULTS AND DISCUSSION

2.1. Probable Carbon Sources for CO_2 Evolution.

Gaseous CO_2 formation during charge is indicative of parasitic degradation reactions occurring at the DRX cathode—electrolyte interface.[10] When a porous DRX cathode is tested in a typical Li-ion half-cell setup (Figure 1), degradation-derived CO_2 can originate from four probable carbon sources, including solid native carbonate, conductive carbon black, polyvinylidene fluoride (PVdF) binder, and carbonate-based electrolyte solvent. Trace native carbonate (CBN) inevitably remains on the DRX surface after material synthesis,[8,9] because lithium carbonate (Li_2CO_3) in excess stoichiometry is typically used as the Li precursor during solid-state synthesis (see Experimental Section). Previous studies have shown that first-cycle CO_2 outgassing is largely contributed by the decomposition of CBN,[14,15] whose resulting CO_2 evolution is referred to as CBN-CO_2 in this work. Another carbon source for CO_2 in the as-prepared DRX cathode is carbon black (CBK), added to form an electron conduction network in the porous electrode. The oxidation of CBK and its resulting CO_2 outgassing (referred to as CBK-CO_2) are non-negligible in a Li-ion cell charged to a high upper cutoff voltage (>4.5 V),[16] which is usually required for DRX cathodes. On the other hand, high-voltage degradation of the PVdF binder in carbonate-based electrolyte has previously been shown to be insignificant,[17] as PVdF-derived CO or CO_2 (PVdF-CO_2) was not observed. Although we cannot fully rule out the possibility of PVdF-CO_2 evolution from the DRX porous cathode, we posit that its quantity is negligible due to its exceptional stability against oxidation[17,18] and the minimal amount of PVdF-CO_2, if any, is lumped into electrolyte-derived CO_2 (referred to as EC-CO_2) in this study, as shown in Figure 1.

2.2. ^{13}C-Labeled LMTO Cathodes.

To differentiate among CO_2 originating from various carbon sources, we selectively labeled electrode components with the ^{13}C isotope. Three types of ^{13}C-tagged electrodes allow us to isotopically isolate each source of CO_2, as outlined in Table 1. Table 1 also provides our notation for each isotope labeling combination. Specifically, LMTO with trace ^{13}C-enriched CBN was synthesized by substituting the Li-supplying precursor Li_2CO_3 with $Li_2{}^{13}CO_3$ (99 atom % ^{13}C), following the same solid-state synthesis procedure described in our previous work.[19] The as-synthesized LMTO exhibits almost identical X-

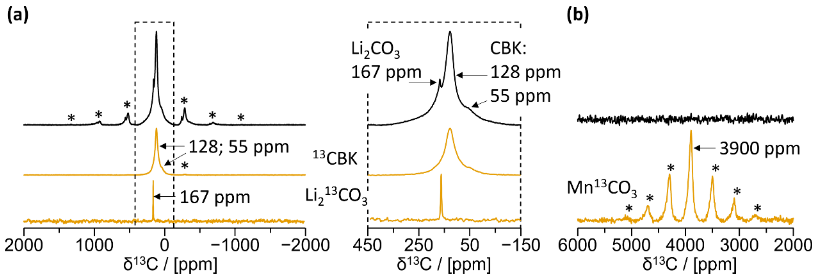

Figure 2. ^{13}C solid-state nuclear magnetic resonance (ssNMR) spectroscopy confirms Li_2CO_3 as the dominant form of residual CBN. (a) ^{13}C ssNMR spectra of 13CBN-13CBK composite powder (black trace, listed in Tables 1 and 2) compared to pure ^{13}C-enriched Li_2CO_3 (orange trace, bottom) and carbon black (CBK, orange trace, middle). The isotropic region 450 to −150 ppm is in dashed black rectangle and highlighted in the right panel. (b) ^{13}C ssNMR of 13CBN-13CBK composite powder (black trace) compared to pure ^{13}C-enriched $MnCO_3$ (orange trace). See Experimental Section for details of isotopic enrichment and magic angle spinning probe conditions. Asterisk symbols indicate spinning sidebands.

Table 2. ^{13}C Enrichment of CBN in Various LMTO-CBK Powders after Ball Milling

LMTO powder[a]	net Li_2CO_3 (μmol g_{LMTO}^{-1})	$Li_2{}^{12}CO_3$ (μmol g_{LMTO}^{-1})	$Li_2{}^{13}CO_3$ (μmol g_{LMTO}^{-1})	^{13}C enrichment (atom %)
13CBN-12CBK	202.1	63.2	138.9	68.7
13CBN-13CBK	206.0	26.0	180.0	87.4
12CBN-13CBK	210.7	120.3	90.4	42.9

[a]These powders were used to prepare LMTO electrodes as outlined in Table 1.

ray diffraction (XRD) patterns and voltage profiles as shown in the Supporting Information (Figures S1 and S2), indicating attainment of the intended rock-salt structure and target composition. The only expected difference lies in the presence of isotope ^{13}C within trace CBN, which we will characterize in the following sections through solid-state nuclear magnetic resonance (ssNMR) spectroscopy and strong acid titration coupled with mass spectrometry.

2.2.1. Li_2CO_3 as the Dominant Form of Solid Native Carbonate. Solid carbonates can exist with the carbonate anion ($CO_3{}^{2-}$) paired to various metal cations, which can be Li or Mn during the synthesis of the LMTO material. Here, titanium carbonate is ruled out since it is not a thermodynamically stable phase and not found in any of the major material databases, e.g., the Inorganic Crystalline Structure Database (ICSD)[20] and the Materials Project.[21] While lithium and manganese carbonates possess distinct crystal structures, detecting trace amounts of potentially amorphous carbonate impurities (<2 wt %) in DRX cathode samples is challenging with XRD. Here, we exploit ^{13}C ssNMR spectroscopy (Figure 2) to probe and discern ^{13}C-enriched Li_2CO_3 and $MnCO_3$ impurity phases, as well as ^{13}C-enriched CBK, in a LMTO composite powder (referred to as 13CBN-13CBK in Table 2). The ^{13}C ssNMR spectrum obtained on a reference ^{13}C-enriched Li_2CO_3 sample exhibits a sharp resonance at ∼167 ppm (bottom orange trace in Figure 2a), and that collected on a reference ^{13}C-enriched CBK (13CBK) sample has two resonances at 128 and 55 ppm (middle orange trace in Figure 2a), broadened by the large number of ^{13}C environments in the disordered carbon structure. The ssNMR spectrum obtained on ^{13}C-enriched $MnCO_3$ contains a very broad and highly shifted signal centered at 3900 ppm (orange trace in Figure 2b) resulting from the strong paramagnetic interactions between unpaired electron spins originating from nearby Mn^{2+} d orbitals and the ^{13}C nuclear spins under observation. Further, fast spinning of the $MnCO_3$ sample during ssNMR data acquisition leads to a manifold of spinning sidebands on either side of the centerband.

Moving on to the 13CBN-13CBK composite cathode of interest, its ^{13}C ssNMR spectrum recorded over the −2000 to 2000 ppm range exhibits a broad signal around 100 ppm with multiple spinning sidebands (black trace in Figure 2a left). Focusing on the isotropic region from 450 to −150 ppm (black trace in Figure 2a right), three overlapping signals can be distinguished at 167, 128, and 55 ppm. The signal at 167 ppm is attributed to an Li_2CO_3 impurity, while the two signals at 128 and 55 ppm correspond to CBK. The presence of multiple sidebands in the ^{13}C ssNMR spectrum collected on the composite cathode result from the close proximity of the Li_2CO_3 and 13CBK phases with the paramagnetic DRX phase, leading to long-range paramagnetic (electron−nuclear spin dipolar) interactions and signal broadening. We note that quantifying the amount of Li_2CO_3/CBK phases in the samples of interest using ^{13}C ssNMR is challenging due to uncertainties regarding the actual ^{13}C enrichment of CBK powder. On the other hand, the ^{13}C ssNMR spectrum recorded in the 4000 ppm region (black trace in Figure 2b) does not show any sign of $MnCO_3$ impurity in the cathode, which further confirms that Li_2CO_3 is the dominant form in residual CBN.

2.2.2. ^{13}C Enrichment in Solid Native Carbonate. Residual CBN has been shown to be quantifiable by the previously established titration mass spectrometry (TiMS) technique.[9,22,23] Disintegrating solid Li_2CO_3 in strong aqueous acid leads to characteristic CO_2 release, which can be accurately analyzed by a mass-spectrometry (MS) gas analyzer:

$$\begin{aligned} &Li_2^{*}CO_3(s) + 2H_3O^+(aq) \\ &\quad \rightarrow 2Li^+(aq) + 3H_2O(l) + {}^{*}CO_2(g) \end{aligned} \tag{1}$$

Here the asterisk symbol denotes partial ^{13}C enrichment, which is also measurable by TiMS. Upon titrating the LMTO powder that is expected to contain trace CBN enriched with ^{13}C (Figure 3a), we observed TiMS CO_2 evolution with a substantially greater amount of $^{13}CO_2$ than $^{12}CO_2$, which indicates CBN with a high ^{13}C enrichment level at 94.4 atom %. Interestingly, the ^{13}C enrichment decreases to 68.7 atom % (Figure 3b) after the as-synthesized LMTO powder is mixed

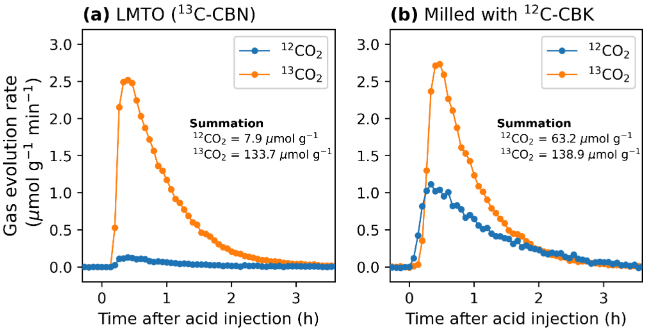

Figure 3. Quantification of ^{13}C-enriched native carbonate (CBN) through titration mass spectrometry (TiMS), following eq 1. (a) CO_2 evolution curves from titrating LMTO powder synthesized from $Li_2{}^{13}CO_3$, thereby containing residual trace ^{13}C-CBN. (b) CO_2 evolution curves from titrating the same LMTO powder shaker-milled with natural isotope abundance carbon black (^{12}C-CBK). The *y*-axis unit represents molar gas evolution rate per gram of active material LMTO, excluding carbon black. Integration of each peak provides the total carbonate amount in a given sample in μmol g_{LMTO}^{-1}.

and shaker-milled with ^{12}C-CBK powder in a jar sealed under an argon atmosphere. As shown in Figure 3a,b, the amount of ^{13}C-CBN remains similar after mixing with ^{12}C-CBK, while the ^{12}C-CBN content increases substantially and accounts for ~30 mol % of net CBN in the electrode material referred to as 13CBN-12CBK in Table 1. Similarly, we observed unintended ^{13}C-CBN in the 12CBN-13CBK electrode. The amounts and isotopic carbon distributions of CBN (quantified through eq 1) in various LMTO electrodes are summarized in Table 2. It should be noted that even with additional unintended CBN formation, the overall CBN impurity is still in a trace amount (<2 wt % of the active material, LMTO material + trace CBN). Although we cannot rule out the possibility of material's exposure to a limited amount of ambient CO_2 during the handling, our results clearly suggest that mechanical milling of DRX materials with CBK contributes to a non-negligible amount of CBN, implying that carbon of CBK reacts with lithium and oxygen at the surface of LMTO, in the as-prepared cathode. This suggestion is bolstered by the sizable reduction of $Li_2{}^{12}CO_3$ in the 13CBN-13CBK electrode compared to that in the 13CBN-12CBK electrode (i.e., shaker-milling with ^{13}C carbon black results in less $Li_2{}^{12}CO_3$ and more $Li_2{}^{13}CO_3$ formation, indicating that the carbon black is in fact the carbon source for the additional carbonate rather than, e.g., air contamination). Most importantly, the quantitative information on ^{13}C-enriched CBN will enable us to distinguish in situ CO_2 evolved from different carbon sources during the battery operation.

2.3. Time-Dependent in Situ CO_2 Evolution Analysis.

In situ monitoring of CO_2 outgassing is critical to correlate cathode−electrolyte interface degradation with DRX cathode electrochemical performance.[10] For LMTO cathodes with various ^{13}C-labeled carbon sources (Table 1), $^{12}CO_2$ and $^{13}CO_2$ can evolve concurrently, and their relative contributions may change at different states of charge (SOC) due to the varying extent of degradation in each carbon source. To quantitatively analyze the mixture of $^{12}CO_2$ and $^{13}CO_2$ outgassing, we performed DEMS with ^{13}C-labeled LMTO cathodes in a carbonate-based electrolyte. The mass-to-charge ratio (m/z) difference enables us to distinguish $^{12}CO_2$ (primary m/z = 44) and $^{13}CO_2$ (primary m/z = 45) in the MS signals. As the MS fragmentation of the linear carbonate vapor (e.g., dimethyl carbonate) contributes substantially to the MS signal at m/z = 45, here we used ethylene carbonate (EC) as the single solvent to eliminate the volatility of the electrolyte and reduce its interference with the detection of $^{13}CO_2$, which has the primary MS signal at m/z = 45. EC is known to primarily contribute to high-voltage electrolyte instabilities in mixed-carbonate solvents,[24] such that studying EC by itself provides valuable insight into gas evolution signatures during cell operation in such electrolytes.

2.3.1. Substantial CO_2 Evolution from Residual Native Carbonate (CBN-CO_2) in the First Three Cycles.

Figure 4a

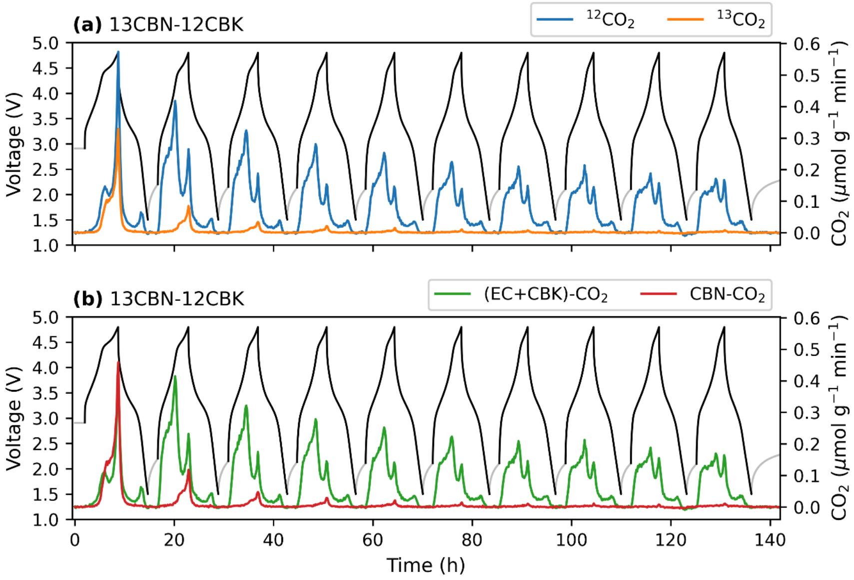

Figure 4. CBN-CO_2 outgassing sources from the 13CBN-12CBK cathode. (a) Isotopic CO_2 evolution from a 13CBN-12CBK cathode (Table 1, LMTO:CBK = 62:28 wt/wt) cycled at the rate of 0.1 mol *e* mol^{-1} h^{-1} (32.9 mA g^{-1}) between 4.8 and 1.5 V. (b) Decoupled CO_2 evolution based on results in (a), eq 2, and ^{13}C enrichment (Table 2). Gray lines denote open-circuit voltages (OCV) between cycles. The amount of CO_2 is normalized to the mass of active material (LMTO).

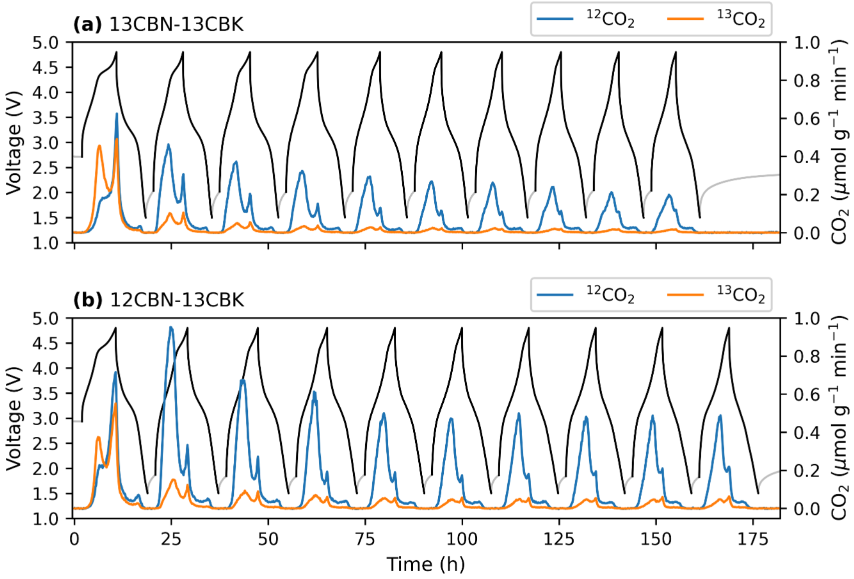

Figure 5. EC-CO_2 reappears from cycle-to-cycle and dominates CO_2 evolution throughout cycling. (a) Isotopic CO_2 evolution from a 13CBN-13CBK cathode (Table 1, LMTO:CBK = 70:20 wt/wt) cycled at the rate of 0.1 mol e mol^{-1} h^{-1} (32.9 mA g^{-1}) between 4.8 and 1.5 V. EC-CO_2 contributes nearly exclusively to $^{12}CO_2$ evolution. (b) Isotopic CO_2 evolution from a 12CBN-13CBK cathode (Table 1, LMTO:CBK = 62:28 wt/wt). CBK-CO_2 contributes nearly exclusively to $^{13}CO_2$ evolution. Gray lines denote open-circuit voltages (OCV) between cycles. The amount of CO_2 is normalized to the mass of active material (LMTO).

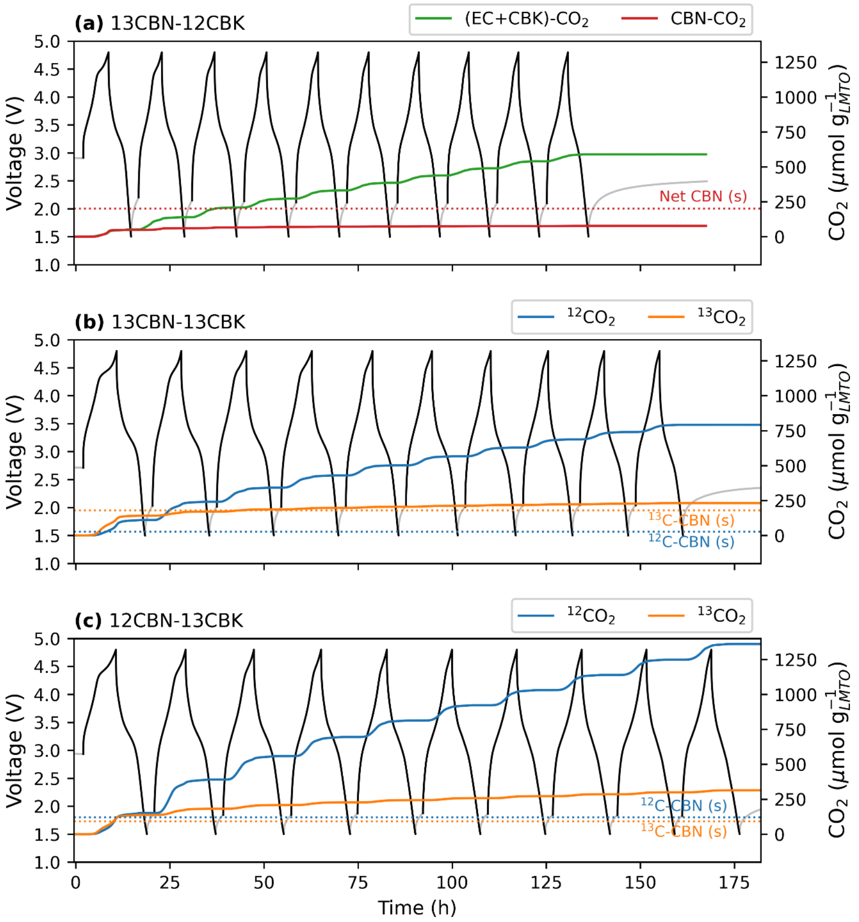

Figure 6. Comparison between the initial ^{13}C-CBN content and cumulative $^{13}CO_2$ suggests non-negligible contribution of CBK-CO_2. (a) Cumulative CO_2 evolution from a 13CBN-12CBK cathode, based on the decoupled data from Figure 4b. (b) Cumulative CO_2 evolution from a 13CBN-13CBK cathode (EC-CO_2 contributes nearly exclusvIely to $^{12}CO_2$ evolution). (c) Cumulative CO_2 evolution from a 12CBN-13CBK cathode (CBK-CO_2 contributes nearly exclusively to $^{13}CO_2$ evolution). The horizontal dotted lines mark the initial amounts of solid native carbonate in μmol g_{LMTO}^{-1}.

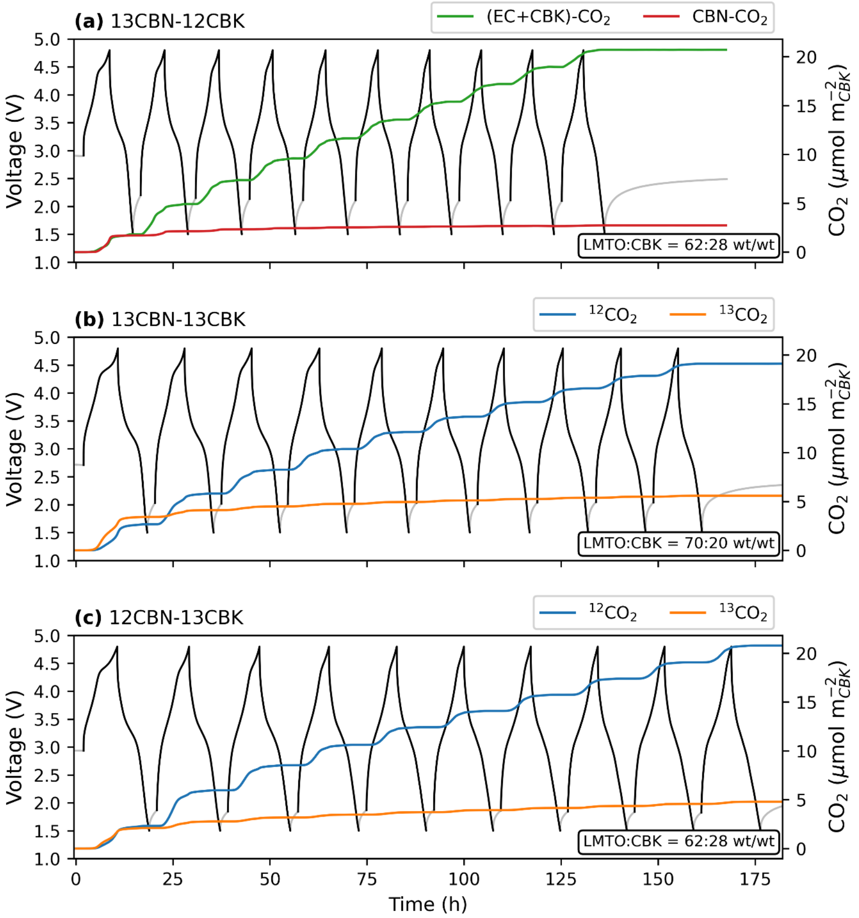

Figure 7. Strong correlation between the total surface area of CBK and cumulative EC-CO$_2$ over 10 cycles. (a) Cumulative CO$_2$ evolution from a 13CBN-12CBK cathode, normalized to the surface area of ^{12}C-CBK (Super C65 and Super P, BET surface area of ≈63 m^2 g^{-1}).[28] (b) 13CBN-13CBK data normalized to the surface area of ^{13}C-CBK (Sigma-Aldrich, BET surface area = 145 m^2 g^{-1}).[17] (c) 12CBN-13CBK data normalized to the surface area of ^{13}C-CBK. All cathodes were cycled at the rate of 0.1 mol e mol^{-1} h^{-1} (32.9 mA g^{-1}) between 4.8 and 1.5 V. Gray lines denote open-circuit voltages (OCV) between cycles.

displays ^{12}CO$_2$ and ^{13}CO$_2$ outgassing data from the 13CBN-12CBK cathode cycled at a constant current rate of 0.1 mol e mol^{-1} h^{-1} (moles of electrons passed per hour per mole of active material LMTO, equivalent to 32.9 mA g^{-1}) between 1.5 and 4.8 V. In the 13CBN-12CBK cell, because ^{13}C-CBN is the only ^{13}C source (natural abundance of ^{13}C in ^{12}C-CBK and ^{12}C-EC is assumed negligible), we attribute all ^{13}CO$_2$ to CBN-CO$_2$. In addition to the fact that all ^{13}CO$_2$ molecules originate from ^{13}C-CBN, the solid-phase ^{13}C enrichment obtained from TiMS (Figure 3b and Table 2) allows us to strictly decouple CO$_2$ into CBN-CO$_2$ and (CBK+EC)-CO$_2$ by the following equations:

$$N_{\text{CBN-CO}_2} = \frac{N_{^{13}\text{CO}_2}}{r_{13\text{CBN}}} \tag{2}$$

$$(N_{\text{CBK-CO}_2} + N_{\text{EC-CO}_2}) = (N_{^{12}\text{CO}_2} + N_{^{13}\text{CO}_2}) - N_{\text{CBN-CO}_2} \tag{3}$$

Here N_i is the molar amount of gas species i and $r_{13\text{CBN}}$ is the ^{13}C enrichment of solid CBN. As shown in Figure 4b, CBN-CO$_2$ contributes to more than half of the net CO$_2$ outgassing (53.5 mol %) in the first cycle, but it diminishes drastically in the following cycles (12.6 mol % in the second cycle; 6.3 mol % in the third cycle). The total cumulative CBN-CO$_2$ evolved over the first 10 cycles, as calculated by integrating the CBN-CO$_2$ evolution in Figure 4b, is only ~40 mol % of the CBN originally contained in the electrode (Table 2), which implies that a portion of solid CBN is electrochemically[13,15] or chemically[25,26] insulated from decomposition reactions. In summary, the 13CBN-12CBK result suggests that the removal of the CBN impurity in DRX materials may help reduce in situ CO$_2$ outgassing during the first few (formation) cycles. After three cycles, the contribution of CBN-CO$_2$ becomes <5 mol % of all CO$_2$ sources, while (CBK+EC)-CO$_2$ reappears during every charge. We now further distinguish CBK-CO$_2$ from EC-CO$_2$ by using the other two sets of ^{13}C-labeled electrodes.

2.3.2. Repetitive CO$_2$ Evolution from Electrolyte Solvent Degradation (EC-CO$_2$) Dominates over Cycling. The 13CBN-13CBK cathode in Table 1 is intended for the investigation of CO$_2$ originating from interfacial electrolyte decomposition (i.e., the electrolyte is the predominant ^{12}C-labeled carbon source, which is now isolated with all other carbon sources being ^{13}C-labeled). As shown in Figure 5a, when the 13CBN-13CBK cathode is charged in each individual cycle, ^{12}CO$_2$ evolves repeatedly, which we attribute mainly to EC-CO$_2$. It is noteworthy that we cannot use analogous calculations in eqs 2 and 3 to strictly deconvolute CO$_2$ into EC-CO$_2$ and (CBN+CBK)-CO$_2$ for the 13CBN-13CBK cathode, because there exists a slight amount of ^{12}C-CBN

(Table 2). Despite this limitation in the 13CBN-13CBK electrode, we confirm EC-CO_2 as the main contributor to $^{12}CO_2$ by comparing two quantities: the cumulative amount of $^{12}CO_2$ and the initial amount of solid ^{12}C-CBN (measured by TiMS; Table 2), as shown in Figure 6b. In the first cycle, the cumulative amount of $^{12}CO_2$ evolved clearly outgrows ^{12}C-CBN that initially exists in the 13CBN-13CBK cathode, indicating that the other ^{12}C source (electrolyte EC) must contribute substantially: $^{12}CO_2 \approx$ EC-CO_2 and $^{13}CO_2 \approx$ (CBN+CBK)-CO_2 in Figure 5a and Figure 6b.

In contrast to the recurring low-voltage activities of EC-CO_2 generation, EC-CO (^{12}CO from 13CBN-13CBK) evolution near the low-voltage range attenuates quickly over the first three cycles, as shown in Figure S3. Recurring EC-CO is largely associated with the high-voltage degradation process, which agrees with the established EC degradation mechanisms involving both CO and CO_2 outgassing.[16,25] In addition, trace H_2 also evolves near the top of the charge, which is likely to originate from protic species generated from the DRX cathode degradation and subsequently diffusing to the Li anode.[10] In the opposite crossover direction to the cathode, the oxidation of EC degradation products from the lithium anode cannot be fully ruled out in our electrochemical cell setup. However, its contribution to EC-CO_2 is likely to be limited as has been observed by another research group.[27] Specifically, swapping lithium metal with delithiated lithium iron phosphate has been shown to have negligible impact on the second-cycle CO_2 evolution (Figure 3D in ref 27) for a different Li-excess cathode material with comparable areal active material loading tested in the carbonate-based electrolyte, which indicates that Li metal plays a minor role in CO_2 evolution from EC degradation.

After the first cycle, EC-CO_2 becomes predominant over other types of CO_2 outgassing, which suggests that improving the electrolyte instability would be the most effective strategy to mitigate CO_2 outgassing from LMTO cathodes. With the fact that EC-$CO_2 \gg$ (CBN+CBK)-CO_2 over cycling, it becomes clear that the cumulative (CBK+EC)-CO_2 in Figure 6a is mostly contributed by EC-CO_2 after 10 cycles. When comparing the blue trace ending point in Figure 6b to the green trace ending point in Figure 6a, we observed a higher net amount of EC-CO_2 from the 13CBN-13CBK cathode than net (CBK+EC)-CO_2 from the 13CBN-12CBK cathode. We suspect that the disparity is most likely due to the different surface areas of the CBKs used in the two electrodes according to the following reasoning.

The battery-grade ^{12}C-CBK (Super C65 and Super P) has a BET surface area of ~63 $m^2\ g^{-1}$,[28] while ^{13}C-enriched CBK was reported to have a BET surface area of 145 $m^2\ g^{-1}$.[17] If the cumulative gas evolution is normalized to the total surface area of the CBK contained in each electrode (in units of μmol m_{CBK}^{-2}; Figure 7a,b), the cumulative CO_2 evolved from electrolyte degradation during 10 cycles is similar in both the 13CBN-12CBK ((CBK+EC)-$CO_2 \approx$ EC-CO_2) and 13CBN-13CBK ($^{12}CO_2 \approx$ EC-CO_2) electrodes. Furthermore, we intentionally varied the ^{13}C-CBK content between the 13CBN-13CBK (20 wt % of CBK) and 12CBN-13CBK (28 wt % of CBK) cathodes (Figure 7b,c), with higher CBK content showing a greater net μmol g_{LMTO}^{-1} of $^{12}CO_2$, but again a similar net μmol m_{CBK}^{-2} of $^{12}CO_2$ ($\approx$EC-CO_2) after 10 cycles. The difference in μmol g_{LMTO}^{-1} of $^{12}CO_2$ is much greater than the difference in ^{12}C-CBN between blue dotted lines in Figure 6b,c, which indicate that the increase of $^{12}CO_2$ outgassing from 12CBN-13CBK is in fact contributed by EC-CO_2 rather than CBN-CO_2. This analysis has a critical implication: EC degradation processes involving EC-CO_2 outgassing at the DRX cathode−electrolyte interface are strongly correlated with the total surface area of electron-conducting CBK, which we will investigate further in a later section (2.4. Voltage-Dependent Differential Analysis) after discussing whether there is any CO_2 outgassing originating from CBK.

2.3.3. Non-Negligible CO_2 Evolution from Carbon Black Degradation (CBK-CO_2).

CBK-CO_2 is investigated through DEMS measurements with the 12CBN-13CBK cathode as listed in Table 1. Although the existence of ^{13}C-CBN (Table 2) prevents deconvolution of CO_2 into CBK-CO_2 and (CBN+EC)-CO_2 for the 12CBN-13CBK cathode, the cumulative amount of $^{13}CO_2$ exceeds ^{13}C-CBN in the first cycle and continues to grow during cycling (Figure 6c), which confirms the non-negligible contribution of CBK-CO_2. With evidence of CO_2 originating from CBK, our DEMS results further reveal an interesting CBK-CO_2 evolution pattern, which is especially pronounced in the first cycle. When comparing Figure 4b and Figure 5a,b, we observed two distinct peaks of CBK-CO_2 evolution in the first cycle. The two-peak pattern reappears with diminishing amounts in the following cycles, as shown in Figure 5b. As the CBK-CO_2 evolves in both low-voltage and high-voltage ranges, we will further apply differential analysis to the DEMS data to better visualize and identify the onset voltages of the multimodal CO_2 evolution.

2.4. Voltage-Dependent Differential Analysis.

Differential analysis is a typical data processing technique to convert galvanostatic, i.e., constant-current (usually time-dependent or capacity-dependent) results into voltage-dependent results. For example, differential capacity analysis quantifies the major redox voltage distribution by taking the derivative of capacity q against the measured voltage V, which is commonly called $dq\,dV^{-1}$ analysis.[19] Although differential analysis against V is suitable to quantify the major redox contributions, $dN_i\,dV^{-1}$ (N_i being moles of evolved gas i) for CO_2 outgassing can result in misleading trends of minor parasitic processes. Specifically, because the galvanostatic voltage profile of the LMTO cathode is largely determined by the delithiation/lithiation of the LMTO material, any voltage plateau feature can fictitiously exacerbate the CO_2 outgassing reactivity in a narrow voltage range on a $dN_i\,dV^{-1}$ plot (Figure S5). Analogously, a steep-slope voltage feature can underestimate the reactivity of parasitic processes over a wide voltage range. To better visualize the relative reactivity of parasitic processes involving CO_2 outgassing during charge at a constant current I, we further derive another differential quantity, $dN_i\,dq^{-1}$:

$$\frac{dN_i}{dq} = \frac{dN_i}{dt}\cdot\frac{1}{\frac{dq}{dt}} = \frac{dN_i}{dt}\cdot\frac{1}{I} \tag{4}$$

Basically $dN_i\,dq^{-1}$ can be evaluated in units of mol (mol e)$^{-1}$, which represents moles of gas species i evolved per moles of electrons passed. The physical meaning of $dN_i\,dq^{-1}$ is very close to that of Faradaic efficiency (FE$_i$), which is scaled by the stoichiometric coefficient ν_{ij} for a specific degradation mechanism j producing a gas species i:

$$FE_i = \sum_j \nu_{ij}\frac{dN_{ij}}{dq} \tag{5}$$

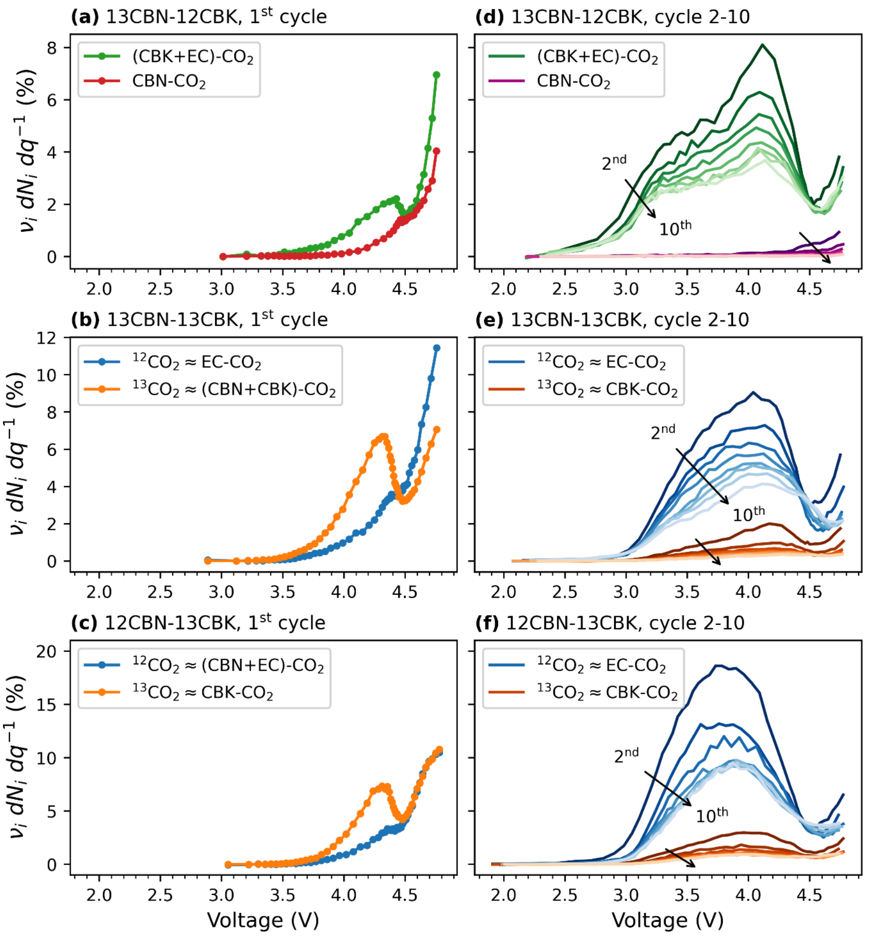

Figure 8. Voltage- and cycle-dependent multimodal CO_2 outgassing. (a−c) First-cycle $\nu_i\,dN_i\,dq^{-1}$ analysis based on eqs 4 and 7−10. (d−f) $\nu_i\,dN_i\,dq^{-1}$ analysis from the second to tenth cycle for each electrode described in Table 1. CBN-CO_2 traces in (d) are plotted at a smaller y-scale in Figure S3 to show the onset.

$$dN_i = \sum_j dN_{ij} \qquad (6)$$

Here multiple degradation mechanisms and reaction routes j can contribute to a certain type of CO_2 evolution and the combination in eq 6 can vary in different voltage windows. Although determining all ν_{ij} and measuring all dN_{ij} are beyond the scope of this study, we posit that most ν_{ij} fall within the range from 2 to 4 based on previously established mechanisms (e.g., $\nu_{ij} = 4$ for i = EC-CO_2 via j = $^1O_2$ oxidation;[25] $\nu_{ij} = 2$ for i = CBN-CO_2 via j = electrochemical oxidation[15]). This underlying knowledge allows us to estimate FE_i by approximating all ν_{ij} as a single ν_i value for each gas i:

$$FE_i \approx \nu_i \frac{dN_i}{dq} \qquad (7)$$

$$\nu_i \approx 2 \quad \text{for } i = \text{CBN-CO}_2 \qquad (8)$$

$$\nu_i \approx 4 \quad \text{for } i = \text{EC-CO}_2 \text{ or CBK-CO}_2 \qquad (9)$$

$$\nu_i \approx 3 \quad \text{for } i = \text{(CBN+CBK)-CO}_2 \text{ or (CBN+EC)-CO}_2 \qquad (10)$$

We expect the approximated $\nu_i\,dN_i\,dq^{-1}$ to be of similar order of magnitude as the exact FE_i, so we will present all $\nu_i\,dN_i\,dq^{-1}$ data in the unit of %, as commonly used for FE_i.

2.4.1. First-Cycle CO_2 Evolution Pattern.

Figure 8 shows the first-cycle $\nu_i\,dN_i\,dq^{-1}$ vs V from the three cathodes listed in Table 1, which enables us to identify the onset voltages of CO_2 outgassing from various carbon sources. From the 13CBN-12CBK cell, (Figure 8a) we observed an onset of CBN-CO_2 at ∼3.9 V, which agrees well with the electrochemical oxidation mechanism demonstrated in electrodes made without cathode materials, but with carbon and Li_2CO_3.[13,15] After CBN-CO_2 onsets, the $dN_{\text{CBN-CO}_2}\,dq^{-1}$ curve is very close to a unimodal exponential shape, which implies that the relevant reaction is likely to follow anodic Butler−Volmer kinetics. Almost identical onset and exponential shape, but with a reducing magnitude, are observed for CBN-CO_2 over cycling (Figure 8d and Figure S6). These agreements imply that the CBN-CO_2 outgassing mechanism in this case is mostly independent of the LMTO−electrolyte interfacial activities.

For the 13CBN-13CBK cell (Figure 8b) its first cycle shows an onset of $^{12}CO_2$ at ∼3.6 V, which is slightly lower than the onset of CBN-CO_2 and together with Figure 6b confirms that here $^{12}CO_2$ is mainly contributed by EC-CO_2. The shape of the $dN_{^{12}CO_2}\,dq^{-1}$ curve is also close to a unimodal exponential. The results from Figure 8a,b suggest that lowering the charging cutoff voltage may be an effective strategy to reduce LMTO cathode's first-cycle CO_2 originating from both native carbonate and electrolyte degradation. However, we observed an additional $^{13}CO_2$ evolution peak at ∼4.3 V, with an onset at

~3.5 V. By comparing $^{13}CO_2$ in the 12CBN-13CBK cell (Figure 8c) with the other two cells, the bimodal CO_2 evolution is obviously originating from CBK. This result is surprising, as previous studies on CBK electrodes (without cathode active materials) have shown that CBK oxidation to CBK-CO_2 in carbonate-based electrolytes exhibits an almost unimodal exponential reactivity with increasing voltages >4.5 V.[16,17] The bimodal outgassing behavior here indicates that the LMTO material surface must participate in CBK degradation and its resulting CBK-CO_2 outgassing. This implication is again confirmed by the reappearance of bimodal CBK-CO_2 during later cycling, (Figure 8e,f) which will be discussed further in the next section.

2.4.2. Onset Shift of EC-CO_2 and CBK-CO_2 after the First Cycle.

Starting from the second cycle (Figure 8d−f), both EC-CO_2 (e.g., $^{12}CO_2$ evolution in 13CBN-13CBK, Figure 8e) and CBK-CO_2 ($^{13}CO_2$ evolution from 12CBN-13CBK in Figure 8f) onset at lower voltages compared to the first cycle. For CBK-CO_2, the bimodal evolution pattern reappears in decreasing intensities, but after the first cycle its earliest onset shifts down from ~3.5 V to ~3.0 V, which is consistently observed for the rest of the cycles. This implies that the LMTO surface reactivity or cathode−electrolyte interfacial chemistry that induces CBK oxidation changes irreversibly after the first full cycle between 4.8 and 1.5 V.

An even more drastic change after the first cycle occurs for electrolyte degradation involving EC-CO_2 evolution. By comparing Figure 8a−c to Figure 8d−f, the onset of EC-CO_2 shifts down nearly 1 V from ~3.6 V to ~2.6 V. In addition, the gas evolution pattern becomes multimodal with the low-voltage (2.6−4.5 V) contribution outgrowing the high-voltage (>4.5 V) outgassing, as shown in Figures 4b and 5. The result suggests that the parasitic reaction mechanisms at the cathode−electrolyte interface involving EC-CO_2 evolution change drastically after the first cycle.

Although the amount of EC-CO_2 decreases over cycling, it continues to reappear and dominate the CO_2 outgassing, particularly in the low-voltage region that has an extraordinarily wide range from 2.6 to 4.5 V, whose peak EC-CO_2 evolution rate is not proportional to the LMTO mass but correlated to the total carbon-black surface area (Table S5). Combined with the fact that cumulative EC-CO_2 is proportional to the total surface area of the conductive carbon (Figure 7), the CO_2 evolution onset at 2.6 V implies that soluble EC degradation species, not the EC molecule itself, formed in previous cycles participate in the low voltage chemistry. Efforts are underway to isolate these species, which could further provide insight into electrolyte decomposition mechanisms. In summary, our results indicate that not only high-voltage (>4.5 V) cathode−electrolyte instability but also the low-voltage (2.6−4.5 V) degradation involving currently unknown CBK-CO_2 and EC-CO_2 outgassing mechanisms need to be improved for stable operation of LMTO cathodes.

3. CONCLUSIONS

The chemical origin of the CO_2 outgassing from the LMTO cathodes operated in a carbonate-based electrolyte is strongly voltage- and cycle-dependent. During the first (formation) charge, high-voltage (>4.5 V) CO_2 evolution is contributed by all three carbon sources (CBN, CBK, and EC), while CBK oxidation contributes substantially in the low-voltage range (3.5−4.5 V) as a result of an unusual bimodal CBK-CO_2 evolution pattern. Beyond the first cycle, the parasitic reaction mechanisms at the LMTO−eletrolyte interface change drastically, leading to lower onset voltages of CBK-CO_2 and EC-CO_2 in subsequent cycles. In particular, EC-CO_2 consistently reappears in a wide ~2 V range between 2.6 and 4.5 V. The dominant amount of EC-CO_2 is strongly correlated with the total surface area of CBK, revealing the critical role of electron-conducting CBK in the electrolyte decomposition mechanisms leading to EC-CO_2 evolution. Future improvement of the DRX cathode−electrolyte interface should focus not only on the initial (as-synthesized) active material surface properties but also on how to avoid unstable DRX-CBK, DRX-electrolyte, and CBK-electrolyte interfaces evolved during operation after the first (formation) cycle. Further, identifying the species formed that result in the observed low-voltage CO_2 evolution during cycling would be valuable to inform electrolyte design. Ultimately, we anticipate that this work will help advance the understanding of in situ CO_2 outgassing in LiBs using DRX cathodes and pave the way for the design of more environmentally sustainable, stable, and long-lasting energy storage systems.

4. EXPERIMENTAL SECTION

4.1. Materials Synthesis. A conventional solid-state method was used to synthesize cation-disordered rock salt $Li_{1.2}Mn_{0.4}Ti_{0.4}O_2$ (LMTO). Ordinary Li_2CO_3 (Sigma-Aldrich, 99%) or $Li_2{}^{13}CO_3$ (Sigma-Aldrich, 98% purity, 99 atom % of ^{13}C enrichment) was used as the Li-supplying precursor. For TM components, Mn_2O_3 (Alfa Aesar, 99.9%) and TiO_2 (Alfa Aesar, 99.9%) were used as precursors. An additional 10% Li_2CO_3 was added to offset any potential loss during the high-temperature synthesis process. These precursors were stoichiometrically mixed in ethanol with a Retsch PM 200 planetary ball mill at a rate of 250 rpm for 12 h. Following the milling process, the mixture was dried overnight at 70 °C and then pelletized. These precursor pellets were subsequently heated to 1100 °C at a rate of 9 °C min^{-1} under an argon gas atmosphere, held at 1100 °C for 20 min, and then allowed to cool naturally within the furnace. To confirm long-range phase purity, lab X-ray diffraction studies (Supporting Information Figure S1) were carried out using a Rigaku Miniflex 600, covering a 2θ range of 15−90°. For further analysis, Rietveld refinement was conducted using PANalytical X'pert HighScore Plus software.

4.2. Electrochemical Cell Assembly. To monitor in situ CO_2 evolution, we tested all LMTO cathodes in a modified Swagelok-type cell format.[29] Cathodes were prepared in an Ar-filled glovebox to limit their exposure to ambient atmosphere. LMTO powder (with residual $Li_2{}^{12}CO_3$ or $Li_2{}^{13}CO_3$) was first shaker-milled with carbon black (^{12}C Super C65 from TIMCAL or 99 atom % ^{13}C-enriched carbon from Sigma-Aldrich) in 7:2 weight ratio for 30 min in an argon atmosphere using a SPEX 800 M mixer/mill. Milled LMTO-carbon powder was then mixed with polyvinylidene fluoride (Solef 6010/1001, SOLVAY) solution in *N*-methyl-2-pyrrolidone solvent (NMP, anhydrous, 99.5%, Sigma-Aldrich) to form a slurry in a planetary centrifugal mixer (ARE-310, THINKY Mixer). For the 13CBN-12CBK and 12CBN-13CBK electrodes in Table 1, additional conductive carbon (^{12}C Super P from TIMCAL or ^{13}C carbon from Sigma-Aldrich) and NMP were added. The final solid weight composition was 62% active material, 28% carbon, and 10% binder for 13CBN-12CBK and 12CBN-13CBK electrodes. For the 13CBN-13CBK electrode, the final solid weight composition was 70% active material, 20% carbon, and 10% binder. The slurry was cast onto a stainless-steel mesh (120 mesh, T-316 stainless steel, TWP Inc.), which allows gas to escape in the cell axial direction. After drying on a 120 °C hot plate for an hour, the electrode was cut into 12 mm disks. Cathode disks were further dried overnight under static vacuum at 120 °C in a heated antechamber attached to the glovebox. The loading density ranged between 4.5 and 7.0 mg cm^{-2} for the cathode active material. Cell anodes are lithium disks with a 12 mm diameter (FMC). To avoid a short circuit in each

Swagelok-type cell, a layer of quartz microfiber disc (Whatman QM-A, cytiva) membrane was used as the separator. All cell components were wet with 80 μL of 1 M $LiPF_6$ (Gotion) in ethylene carbonate (EC, BASF) in each cell, and they were assembled in the glovebox. All experiments were tested under room temperature (ranging between 25 and 30 °C).

4.3. Differential Electrochemical Mass Spectrometry. The in situ CO_2 evolution rate from assembled cells was quantified through a custom-built system that handles gas flow from cells to a mass-spectrometry (MS) gas analyzer, which is commonly called differential electrochemical mass spectrometry (DEMS).[29] MS signals are calibrated for O_2 (research grade, Linde) and CO_2 (>99.9%, Linde) in Ar carrier gas (ultrahigh purity, Linde). To avoid interference from ambient air, each DEMS cell was leak-tested before the measurement began. A Bio-Logic VSP-series potentiostat was used to control the current passed through the DEMS cell, while voltages were recorded every 20 s. Every 10 min, accumulated gas in each cell headspace (~100 μL) was purged intermittently using 500 μL pulses of Ar at recorded gas pressures and room temperatures. In situ evolved gas was sent to a holding chamber, where a variable leak valve controls sampled gas flow into an ultrahigh-vacuum chamber for MS analysis.

4.4. Titration Mass Spectrometry. To quantify residual native carbonate by eq 1, a custom-made (Adams & Chittenden, Berkeley, CA) three-neck glass vessel was used, which can be sealed and attached to a similar gas-handling/MS system as our DEMS setup described above; we call this setup and the following procedure titration mass spectrometry (TiMS).[9] Each glass vessel has two necks, a gas inlet and outlet, connected to the gas-handling system via a combination of Ace-Thred adapters (Ace Glass Inc.), perfluoroalkoxy tubes, and Valco column end fittings (VICI AG.). The third glass neck was septum-sealed, (#7 Ace-Thred, 5037-30) which serves as a titrant injection port. LMTO powder was sealed in a titration glass vessel in the glovebox to limit their exposure to the ambient. After attaching the vessel to the TiMS system, we leak-tested and purged the vessel with Ar carrier gas to avoid interference from ambient air. All titrants were Ar-sparged for >2 h to remove residual air dissolved in the aqueous solution. A gastight syringe (VICI, series C syringe with Pressure-Lok side port needle) was used to inject titrant solution, as this syringe design can avoid introducing any air into the vessel upon injection. To disintegrate residual carbonate, we injected 1.5 mL of strong acid titrant, 1 M triflic acid (HSO_3CF_3 (aq)), which was selected due to its extremely negative pK_a and its stable anion chemistry.[19] Gas accumulated in the vessel headspace (~5 mL) was purged by 2 mL of pulsed Ar every 4 min. All swept-out gas samples were subsequently quantified with the MS gas analyzer.

4.5. ^{13}C Solid-State NMR Spectroscopy. $Li_2{}^{13}CO_3$ powder sourced from the vendor (Sigma-Aldrich, 98% purity, 99 atom % of ^{13}C enrichment) was used as the ^{13}C ssNMR reference sample. The other metal carbonate reference sample, $Mn^{13}CO_3$, was prepared by isotopically enriching $MnCO_3$ powder (Sigma-Aldrich, ≥99.9% purity) by adopting a method detailed in our previous studies.[9] 250 mg of $MnCO_3$ powder was sealed in a tube furnace (total volume ≈100 mL) under N_2 at 1 atm and room temperature, with 50 mL of headspace replaced by $^{13}CO_2$ (Sigma-Aldrich, 99 atom % of ^{13}C enrichment). The enclosed $MnCO_3$ powder and gas was heated to 300 °C for 36 h. The ^{13}C enrichment level, 11 atom % of ^{13}C in $MnCO_3$, was quantified by TiMS and carbonate decomposition reaction stoichiometry similar to that in eq 1.

All ^{13}C ss-NMR spectra were recorded at B_0 = 11.75 T (500 MHz for ^{1}H) using a Bruker BioSpin wide bore spectrometer equipped with an Avance II console and a 1.3 mm HX magic angle spinning (MAS) probe tuned to ^{13}C (125.76 MHz). The ^{13}C ss-NMR spectra were obtained at 50 kHz MAS using a rotor synchronized spin echo sequence ($90°-\tau_R-180°-\tau_R-$AQ) with 90°radio frequency pulses of 1.4 μs and no ^{1}H decoupling during data acquisition. ^{13}C ssNMR spectra acquired around 4000 ppm used a short recovery delay of 30 ms and averaged over 85440 and 665600 transients for $Mn^{13}CO_3$ and 13CBN-13CBK, respectively. ^{13}C ssNMR spectra acquired around 0 ppm for $Li_2{}^{13}CO_3$, 13CBK, and 13CBN-13CBK were averaged over 32, 2048, and 261 632 transients with recovery delays of 180 s, 24 s, and 30 ms, respectively. ^{13}C chemical shift was externally referenced to a concentrated solution of ^{13}C-urea in D_2O ($\delta_{iso}(^{13}C)$ = 161.2 ppm). All ss-NMR spectra were processed using Bruker TopSpin 3.6.0 and Dmfit software.[30]

■ ASSOCIATED CONTENT

Supporting Information

The Supporting Information is available free of charge at https://pubs.acs.org/doi/10.1021/acs.chemmater.4c00756.

> XRD patterns, first-cycle voltage profiles, tabulated amount of CO_2 evolution and their estimated capacity contribution in each cycle for Figures 4 and 5, CO and H_2 gas evolution from the cell in Figure 5b, DEMS of 13CBN-12CBK cycled in different voltage range, tabulated second-cycle peak $^{12}CO_2$ in Figure 5, side-by-side comparison of dN_i dq^{-1} and dN_i dV^{-1}, and zoom-in plot of CBN-CO_2 traces in Figure 8d (PDF)

■ AUTHOR INFORMATION

Corresponding Author

Bryan D. McCloskey − *Department of Chemical and Biomolecular Engineering, University of California—Berkeley, Berkeley, California 94720, United States; Energy Storage and Distributed Resources Division, Lawrence Berkeley National Laboratory, Berkeley, California 94720, United States;* orcid.org/0000-0001-6599-2336; Email: bmcclosk@berkeley.edu

Authors

Tzu-Yang Huang − *Department of Chemical and Biomolecular Engineering, University of California—Berkeley, Berkeley, California 94720, United States; Energy Storage and Distributed Resources Division, Lawrence Berkeley National Laboratory, Berkeley, California 94720, United States;* orcid.org/0000-0003-0500-9306

Zijian Cai − *Department of Materials Science and Engineering, University of California—Berkeley, Berkeley, California 94720, United States; Materials Sciences Division, Lawrence Berkeley National Laboratory, Berkeley, California 94720, United States;* orcid.org/0000-0002-4908-3180

Matthew J. Crafton − *Department of Chemical and Biomolecular Engineering, University of California—Berkeley, Berkeley, California 94720, United States; Energy Storage and Distributed Resources Division, Lawrence Berkeley National Laboratory, Berkeley, California 94720, United States;* orcid.org/0000-0001-7228-5576

Raynald Giovine − *Materials Department, University of California—Santa Barbara, Santa Barbara, California 93106, United States; Department of Chemical and Biomolecular Engineering, University of California—Berkeley, Berkeley, California 94720, United States;* Present Address: College of Chemistry, University of California—Berkeley, Berkeley, California 94720, United States

Ashlea Patterson − *Materials Department, University of California—Santa Barbara, Santa Barbara, California 93106, United States; Materials Research Laboratory, University of California—Santa Barbara, Santa Barbara, California 93106, United States*

Han-Ming Hau − *Department of Materials Science and Engineering, University of California—Berkeley, Berkeley, California 94720, United States; Materials Sciences Division,* *Lawrence Berkeley National Laboratory, Berkeley, California 94720, United States*

Justin Rastinejad − *Department of Chemical and Biomolecular Engineering, University of California—Berkeley, Berkeley, California 94720, United States; Energy Storage and Distributed Resources Division, Lawrence Berkeley National Laboratory, Berkeley, California 94720, United States*

Bernardine L. D. Rinkel − *Department of Chemical and Biomolecular Engineering, University of California—Berkeley, Berkeley, California 94720, United States; Energy Storage and Distributed Resources Division, Lawrence Berkeley National Laboratory, Berkeley, California 94720, United States*

Raphaële J. Clément − *Materials Department, University of California—Santa Barbara, Santa Barbara, California 93106, United States; Materials Research Laboratory, University of California—Santa Barbara, Santa Barbara, California 93106, United States;* orcid.org/0000-0002-3611-1162

Gerbrand Ceder − *Department of Materials Science and Engineering, University of California—Berkeley, Berkeley, California 94720, United States; Materials Sciences Division, Lawrence Berkeley National Laboratory, Berkeley, California 94720, United States;* orcid.org/0000-0001-9275-3605

Complete contact information is available at:
https://pubs.acs.org/10.1021/acs.chemmater.4c00756

Notes

The authors declare no competing financial interest.

■ ACKNOWLEDGMENTS

This research was supported by the Assistant Secretary for Energy Efficiency and Renewable Energy, Office of Vehicle Technologies of the U.S. Department of Energy under Contract DE-AC02-05CH11231 through the Disordered Rocksalt Program. T.-Y.H. gratefully acknowledges support collectively from both the Ministry of Education in Taiwan and UC Berkeley College of Chemistry through Taiwan Fellowship Program. The NMR research reported here made use of the shared facilities of the Materials Research Science and Engineering Center (MRSEC) at UC Santa Barbara: Grant NSF DMR-2308708. The UC Santa Barbara MRSEC is a member of the Materials Research Facilities Network (https://www.mrfn.org/).

■ REFERENCES

(1) Heijlen, W.; Franceschi, G.; Duhayon, C.; Van Nijen, K. Assessing the adequacy of the global land-based mine development pipeline in the light of future high-demand scenarios: The case of the battery-metals nickel (Ni) and cobalt (Co). *Resources Policy* **2021**, *73*, 102202.

(2) Fu, X.; Beatty, D. N.; Gaustad, G. G.; Ceder, G.; Roth, R.; Kirchain, R. E.; Bustamante, M.; Babbitt, C.; Olivetti, E. A. Perspectives on Cobalt Supply through 2030 in the Face of Changing Demand. *Environ. Sci. Technol.* **2020**, *54*, 2985−2993.

(3) Yang, Z.; Huang, H.; Lin, F. Sustainable Electric Vehicle Batteries for a Sustainable World: Perspectives on Battery Cathodes, Environment, Supply Chain, Manufacturing, Life Cycle, and Policy. *Adv. Energy Mater.* **2022**, *12*, 2200383.

(4) Lee, J.; Urban, A.; Li, X.; Su, D.; Hautier, G.; Ceder, G. Unlocking the Potential of Cation-Disordered Oxides for Rechargeable Lithium Batteries. *Science* **2014**, *343*, 519−522.

(5) Yabuuchi, N.; Takeuchi, M.; Nakayama, M.; Shiiba, H.; Ogawa, M.; Nakayama, K.; Ohta, T.; Endo, D.; Ozaki, T.; Inamasu, T.; Sato, K.; Komaba, S. High-capacity electrode materials for rechargeable lithium batteries: Li3NbO4-based system with cation-disordered rocksalt structure. *Proc. Natl. Acad. Sci. U.S.A.* **2015**, *112*, 7650−5.

(6) Chen, R.; Ren, S.; Knapp, M.; Wang, D.; Witter, R.; Fichtner, M.; Hahn, H. Disordered lithium-rich oxyfluoride as a stable host for enhanced Li+ intercalation storage. *Adv. Energy Mater.* **2015**, *5*, 1401814.

(7) Clément, R. J.; Lun, Z.; Ceder, G. Cation-disordered rocksalt transition metal oxides and oxyfluorides for high energy lithium-ion cathodes. *Energy Environ. Sci.* **2020**, *13*, 345−373.

(8) Crafton, M. J.; Yue, Y.; Huang, T.-Y.; Tong, W.; McCloskey, B. D. Anion Reactivity in Cation-Disordered Rocksalt Cathode Materials: The Influence of Fluorine Substitution. *Adv. Energy Mater.* **2020**, *10*, 2001500.

(9) Huang, T.-Y.; Crafton, M. J.; Yue, Y.; Tong, W.; McCloskey, B. D. Deconvolution of intermixed redox processes in Ni-based cation-disordered Li-excess cathodes. *Energy Environ. Sci.* **2021**, *14*, 1553−1562.

(10) Crafton, M. J.; Huang, T.-Y.; Yue, Y.; Giovine, R.; Wu, V. C.; Dun, C.; Urban, J. J.; Clément, R. J.; Tong, W.; McCloskey, B. D. Tuning Bulk Redox and Altering Interfacial Reactivity in Highly Fluorinated Cation-Disordered Rocksalt Cathodes. *ACS Appl. Mater. Interfaces* **2023**, *15*, 18747−18762.

(11) Guéguen, A.; Streich, D.; He, M.; Mendez, M.; Chesneau, F. F.; Novák, P.; Berg, E. J. Decomposition of LiPF6 in High Energy Lithium-Ion Batteries Studied with Online Electrochemical Mass Spectrometry. *J. Electrochem. Soc.* **2016**, *163*, A1095.

(12) Jung, R.; Metzger, M.; Maglia, F.; Stinner, C.; Gasteiger, H. A. Oxygen Release and Its Effect on the Cycling Stability of LiNi x Mn y Co z O 2 (NMC) Cathode Materials for Li-Ion Batteries. *J. Electrochem. Soc.* **2017**, *164*, A1361−A1377.

(13) Kaufman, L. A.; McCloskey, B. D. Surface Lithium Carbonate Influences Electrolyte Degradation via Reactive Oxygen Attack in Lithium-Excess Cathode Materials. *Chem. Mater.* **2021**, *33*, 4170−4176.

(14) Renfrew, S. E.; McCloskey, B. D. Residual Lithium Carbonate Predominantly Accounts for First Cycle CO2 and CO Outgassing of Li-Stoichiometric and Li-Rich Layered Transition-Metal Oxides. *J. Am. Chem. Soc.* **2017**, *139*, 17853−17860.

(15) Mahne, N.; Renfrew, S. E.; McCloskey, B. D.; Freunberger, S. A. Electrochemical Oxidation of Lithium Carbonate Generates Singlet Oxygen. *Angewandte Chemie - International Edition* **2018**, *57*, 5529−5533.

(16) Metzger, M.; Walke, P.; Solchenbach, S.; Salitra, G.; Aurbach, D.; Gasteiger, H. A. Evaluating the High-Voltage Stability of Conductive Carbon and Ethylene Carbonate with Various Lithium Salts. *J. Electrochem. Soc.* **2020**, *167*, 160522.

(17) Metzger, M.; Marino, C.; Sicklinger, J.; Haering, D.; Gasteiger, H. A. Anodic Oxidation of Conductive Carbon and Ethylene Carbonate in High-Voltage Li-Ion Batteries Quantified by On-Line Electrochemical Mass Spectrometry. *J. Electrochem. Soc.* **2015**, *162*, A1123.

(18) Fransson, L.; Eriksson, T.; Edström, K.; Gustafsson, T.; Thomas, J. O. Influence of carbon black and binder on Li-ion batteries. *J. Power Sources* **2001**, *101*, 1−9.

(19) Huang, T.-Y.; Cai, Z.; Crafton, M. J.; Kaufman, L. A.; Konz, Z. M.; Bergstrom, H. K.; Kedzie, E. A.; Hao, H.-M.; Ceder, G.; McCloskey, B. D. Quantitative Decoupling of Oxygen-Redox and Manganese-Redox Voltage Hysteresis in a Cation-Disordered Rock Salt Cathode. *Adv. Energy Mater.* **2023**, *13*, 2300241.

(20) Zagorac, D.; Müller, H.; Ruehl, S.; Zagorac, J.; Rehme, S. Recent developments in the Inorganic Crystal Structure Database: theoretical crystal structure data and related features. *J. Appl. Crystallogr.* **2019**, *52*, 918−925.

(21) Jain, A.; Ong, S. P.; Hautier, G.; Chen, W.; Richards, W. D.; Dacek, S.; Cholia, S.; Gunter, D.; Skinner, D.; Ceder, G.; Persson, K.

A. Commentary: The Materials Project: A materials genome approach to accelerating materials innovation. *APL Mater.* **2013**, *1*, 011002.

(22) Ottakam Thotiyl, M. M.; Freunberger, S. A.; Peng, Z.; Bruce, P. G. The Carbon Electrode in Nonaqueous Li−O2 Cells. *J. Am. Chem. Soc.* **2013**, *135*, 494−500.

(23) Renfrew, S. E.; McCloskey, B. D. Quantification of Surface Oxygen Depletion and Solid Carbonate Evolution on the First Cycle of LiNi 0.6 Mn 0.2 Co 0.2 O 2 Electrodes. *ACS Applied Energy Materials* **2019**, *2*, 3762−3772.

(24) Xia, J.; Petibon, R.; Xiong, D.; Ma, L.; Dahn, J. R. Enabling linear alkyl carbonate electrolytes for high voltage Li-ion cells. *J. Power Sources* **2016**, *328*, 124−135.

(25) Rinkel, B. L. D.; Vivek, J. P.; Garcia-Araez, N.; Grey, C. P. Two electrolyte decomposition pathways at nickel-rich cathode surfaces in lithium-ion batteries. *Energy Environ. Sci.* **2022**, *15*, 3416−3438.

(26) Freiberg, A. T. S.; Sicklinger, J.; Solchenbach, S.; Gasteiger, H. A. Li2CO3 decomposition in Li-ion batteries induced by the electrochemical oxidation of the electrolyte and of electrolyte impurities. *Electrochim. Acta* **2020**, *346*, 136271.

(27) Strehle, B.; Kleiner, K.; Jung, R.; Chesneau, F.; Mendez, M.; Gasteiger, H. A.; Piana, M. The Role of Oxygen Release from Li- and Mn-Rich Layered Oxides during the First Cycles Investigated by On-Line Electrochemical Mass Spectrometry. *J. Electrochem. Soc.* **2017**, *164*, A400.

(28) Pfeifer, K.; Arnold, S.; Budak, O.; Luo, X.; Presser, V.; Ehrenberg, H.; Dsoke, S. Choosing the right carbon additive is of vital importance for high-performance Sb-based Na-ion batteries. *Journal of Materials Chemistry A* **2020**, *8*, 6092−6104.

(29) McCloskey, B. D.; Bethune, D. S.; Shelby, R. M.; Girishkumar, G.; Luntz, A. C. Solvents' Critical Role in Nonaqueous Lithium−Oxygen Battery Electrochemistry. *J. Phys. Chem. Lett.* **2011**, *2*, 1161−1166.

(30) Massiot, D.; Fayon, F.; Capron, M.; King, I.; Le Calvé, S.; Alonso, B.; Durand, J.-O.; Bujoli, B.; Gan, Z.; Hoatson, G. Modelling one- and two-dimensional solid-state NMR spectra. *Magn. Reson. Chem.* **2002**, *40*, 70−76.

https://doi.org/10.1021/acs.chemmater.4c00756
Chem. Mater. 2024, 36, 6535−6546